Supplementary Information for

Dual-site surface sulfidation enables efficient $CsPbI_3$ quantum dot light-emitting diodes with ultralow roll-off

Wanying Zhang[1,2], Mengjie Li[1], Yiran Zhao[1], Xuanyang He[1], Tongtong Wang[1], Xinyang Zhang[1], Yingwei Wang[3], Fan Xia[1,4], Keqiang Chen[1,2,*], Guogang Li[1,2,*]

[1]Faculty of Materials Science and Chemistry, China University of Geosciences, Wuhan 430074, P. R. China

[2]Shenzhen Research Institute, China University of Geosciences, Shenzhen 518052, P. R. China

[3]Hunan Key Laboratory of Nanophotonics and Devices, School of Physics and Electronics, Central South University, Changsha 410083, P. R. China

[4]State key Laboratory of Biogeology and Environmental Geology, China University of Geosciences, 388 Lumo Road, Wuhan 430074, P. R. China

Correspondent:

[*] Prof. Keqiang Chen

E-mail: chenkeqiang@cug.edu.cn

Prof. Guogang Li

E-mail: ggli@cug.edu.cn

Supplementary Note 1.

Discussion on the dual-site surface sulfidation induced $(H_2S)_2$ dimer.

XPS analysis confirms a time-dependent rise in sulfur content (Supplementary Fig. 7d). The newly incorporated H_2S could potentially occupy either the X- or A-site (the latter being theoretically plausible, as suggested by Supplementary Fig. 9). Occupation of additional X-sites would effectively increase the H_2S concentration. This scenario is ruled out because deliberately raising the H_2S concentration severely quenches PLQY (Supplementary Fig. 1c)—a trend opposite to our experimental results (Supplementary Fig. 2). Therefore, the incremental H_2S does not predominantly occupy the X-site.

Concurrently, spectroscopic data (XPS/FTIR/NMR) corroborate a pronounced temporal decrease in native ligand density (Supplementary Figs. S7e, S8), indicating that the incremental H_2S occupies the A-site. This mechanism is further supported by theoretical calculations (Fig. 1e), which demonstrate that an H_2S molecule adsorbed at an X-site promotes the adsorption of another H_2S at a neighboring A-site. These molecules form an $(H_2S)_2$ dimer with significant charge transfer (generating H_3S^+ and HS^-), which stabilizes A-site adsorption and synergistically enhances the binding energy for dual X- and A-site passivation, ultimately leading to a complete and robust surface reconstruction of the QDs.

Supplementary Note 2.

Measurement of ion migration activation energy (E_a).

The E_a was characterized using a custom-built measurement system comprising a Keithley 2400 source meter and a temperature-controlled stage. LEDs fabricated from control and treated QDs were mounted on the stage inside a nitrogen glovebox without encapsulation. Before each measurement, devices were stabilized for 5 minutes at set temperatures ranging from 273 to 308 K. Current densities were sequentially recorded at 0 V, 4 V (forward bias), and again at 0 V, each for durations of 30 s, 50 s, and 30 s, respectively. The resulting current decay profiles were fitted with an exponential function, $I(t) = I_0 + I_1\exp(-t/\tau)$, where the decay rate $k = \tau^{-1}$ reflects ion transport dynamics and is directly related to ionic conductivity. The E_a was subsequently determined from the Arrhenius relation:

$$\ln(kT) = C - \frac{E_a}{k_B T} \quad (1)$$

where T denotes the temperature, C is a constant, k_B is the Boltzmann constant.

Supplementary Note 3.

Theoretical calculations of k_{exciton} and k_{trap}.

Under steady-state excitation, the photoluminescence quantum yield (PLQY) follows the established model:

$$\text{PLQY}(N) = \frac{k_{exction}+N\times k_2}{k_{exction}+k_{trap}+N\times k_2+N^2\times k_3} \quad (2)$$

where the total monomolecular decay rate (k_1) is given by:

$$k_1 = k_{exction} + k_{trap} \quad (3)$$

when electron and hole densities are equal, the carrier rate equation simplifies to:

$$\frac{1}{\tau} = k_1 + N \times k_2 + N^2 \times k_3 \quad (4)$$

Here, N denotes the carrier density; k_{exciton} and k_{trap} represent the rate constants for radiative exciton recombination and trap-assisted nonradiative decay, respectively; k_2 and k_3 correspond to bimolecular radiative and Auger recombination coefficients. The PLQY depends strongly on N, reflecting the competition between these distinct recombination channels. At low excitation densities, first-order processes dominate, where radiative exciton recombination competes primarily with trap-assisted decay. As N increases, bimolecular radiative recombination grows in influence, whereas at high carrier densities, third-order Auger recombination prevails and leads to a marked decline in PLQY.

Under low excitation conditions, where terms involving k_2 and k_3 become negligible, Equations (2) and (4) reduce to simplified forms that highlight the dominance of monomolecular processes:

$$\text{PLQY}(N) = \frac{k_{exction}}{k_{exction}+k_{trap}} \quad (5)$$

$$\frac{1}{\tau} = k_{exction} + k_{trap} \quad (6)$$

It should be noted that the apparent non-radiative recombination rate k_{trap} extracted from Eq. (2) does not necessarily represent the intrinsic non-radiative rate of the system, due to the presence of intermittently "dark" emitters in the ensemble. In quantum-confined perovskite systems, individual emitters may undergo temporary photoluminescence quenching (blinking) before recovering to the emissive state,

maintaining a statistically steady dark fraction over time. Consequently, the experimentally derived k_{trap} includes contributions not only from genuine non-radiative processes (e.g., trap-assisted recombination) but also from variations in the dark fraction. If the dark fraction remains relatively constant across samples, the apparent k_{trap} can still serve as a valid indicator of relative non-radiative changes. Therefore, trends in PLQY derived from Eq. (2) can be reasonably interpreted as reflecting changes in the balance among excitonic, trap-assisted, and Auger recombination pathways, while acknowledging the potential influence of blinking-induced emissive heterogeneity.

Supplementary Note 4.

Calculations of carrier density and carrier recombination coefficients

The initial carrier density (n_0) after pulsed excitation can be estimated using the following equation:

$$n_0 = \frac{a \cdot P}{E_{ph} \cdot f} \cdot \frac{1}{\pi(\frac{d}{2})^2 \cdot t} \quad (6)$$

where a, P, E_{ph}, f, d, and t represent the absorption of perovskite films, laser power, the photon energy, laser repetition rate, full width at half maximum (FWHM) of the Gaussian beam, and the thickness of perovskite films, respectively.

The carrier recombination dynamics can be described by the following rate equation:

$$-\frac{dN(t)}{dt} = aN(t) + bN(t)^2 + cN(t)^3 \quad (7)$$

where $N(t)$ denotes the time-dependent charge carrier density, and a, b, and c correspond to the coefficients of monomolecular recombination, bimolecular recombination, and Auger recombination rates, respectively.

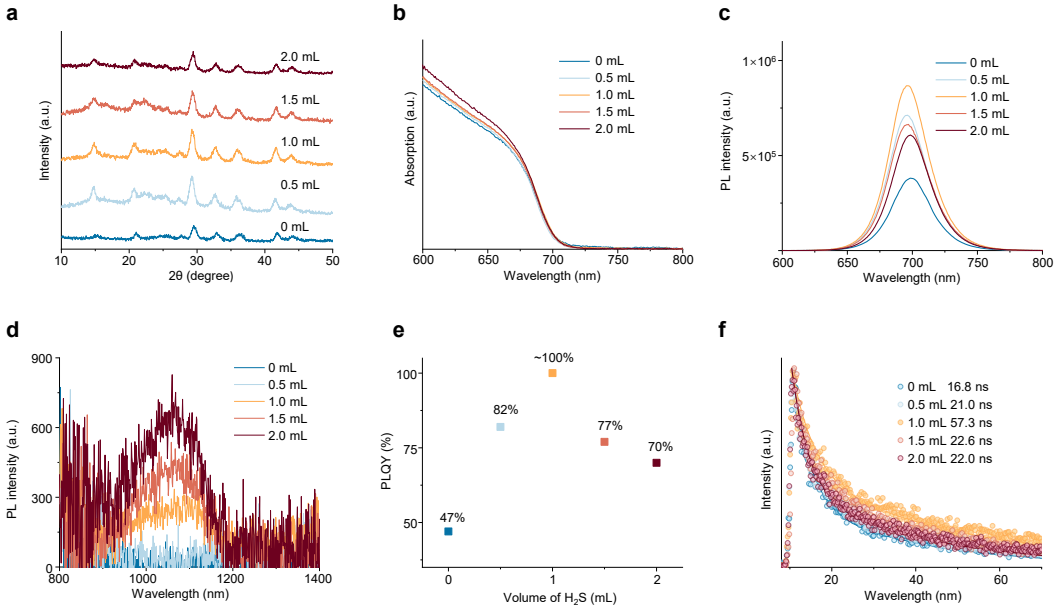

Supplementary Fig. 1 | Dosage-dependent effects of H_2S on $CsPbI_3$ QDs. (**a**) XRD patterns. (**b**) UV absorption spectra. (**c**) PL spectra. (**d**) Near-infrared PL spectra. (**e**) PLQY. (**f**) TRPL spectra. The H_2S modification preserves the original crystal structure while markedly altering optical characteristics. Appropriate treatment achieves effective defect passivation with dramatically improved PLQY and extended PL lifetime, whereas over-sulfurization induces PbS formation and new defect states.

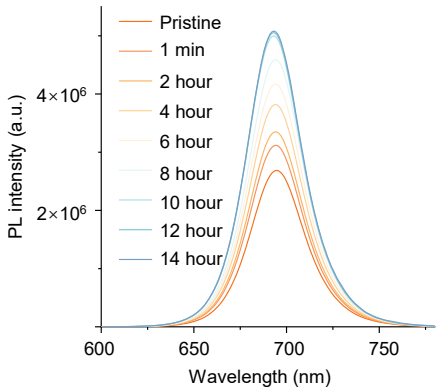

Supplementary Fig. 2 | Time-dependent effects. PL spectra of $CsPbI_3$ QDs with various sulfurization time.

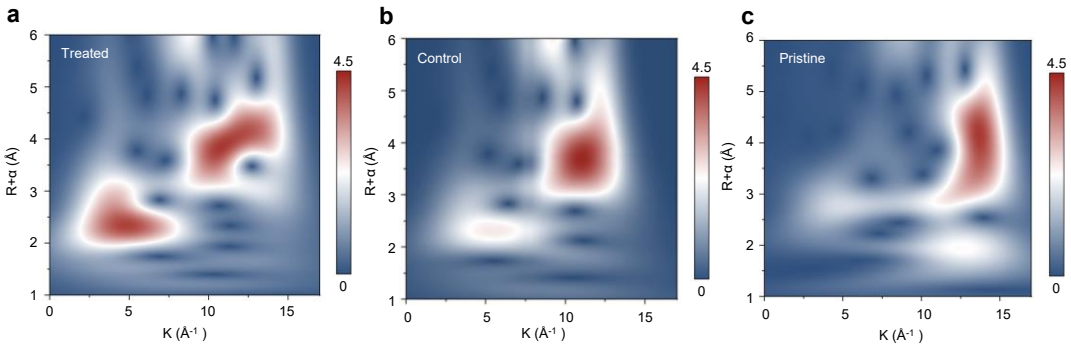

Supplementary Fig. 3 | Wavelet transform plots of $CsPbI_3$ QDs: (**a**) pristine, (**b**) control, (**c**) treated.

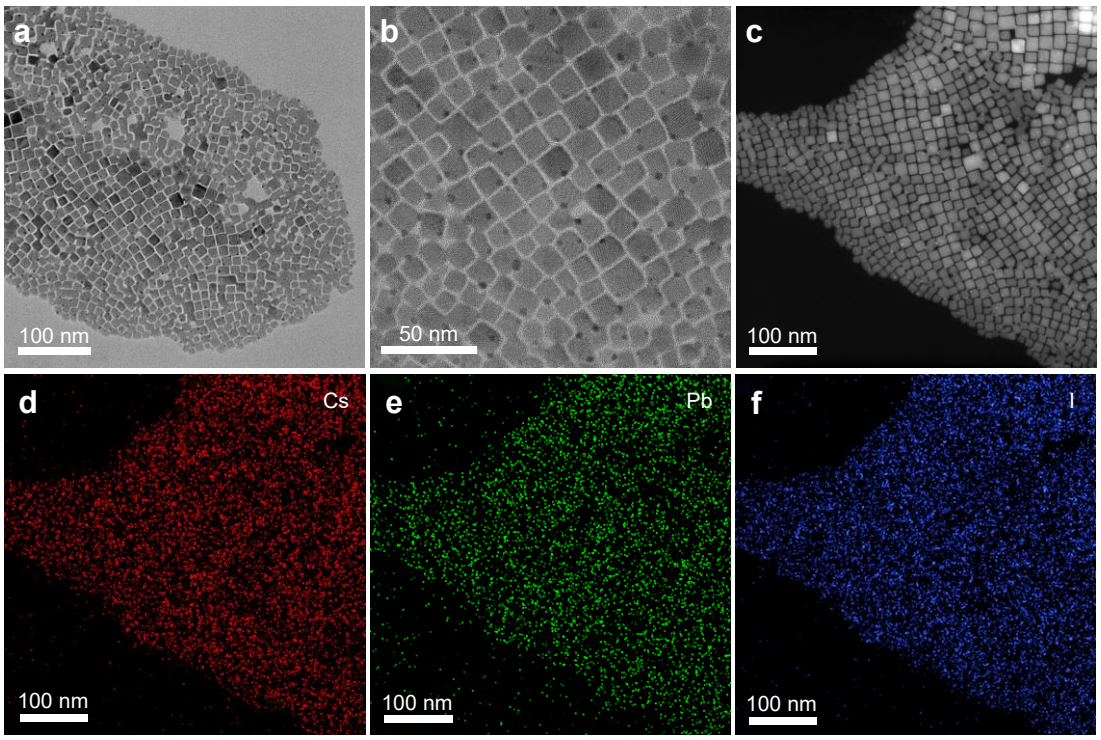

Supplementary Fig. 4 | Morphological characterization of pristine $CsPbI_3$ QDs. (**a** to **c**) (a) TEM, (b) HR-TEM, (c) HAADF-STEM images of pristine QDs. (**d** to **f**) EDS mapping of (d) Cs, (e) Pb, and (f) I.

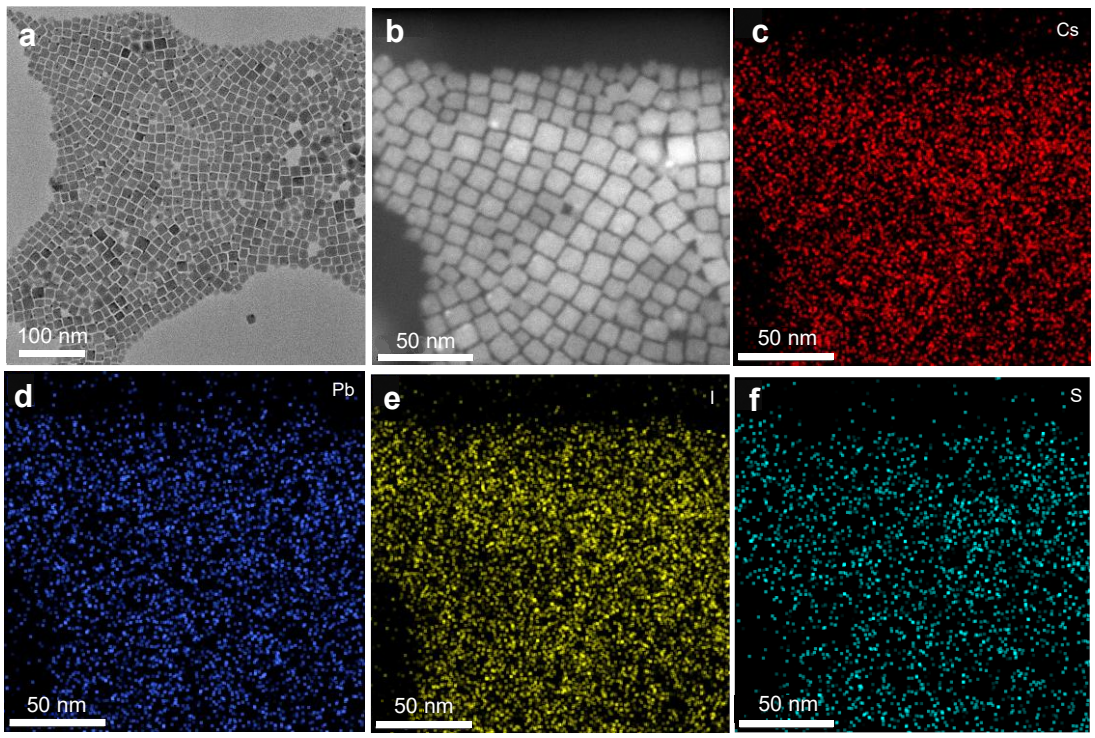

Supplementary Fig. 5 | Morphological characterization of control $CsPbI_3$ QDs. (**a** and **b**) (a) TEM and (b) HAADF-STEM images of control QDs. (**c** to **f**) EDS mapping of (c) Cs, (d) Pb, (e) I, and (f) S.

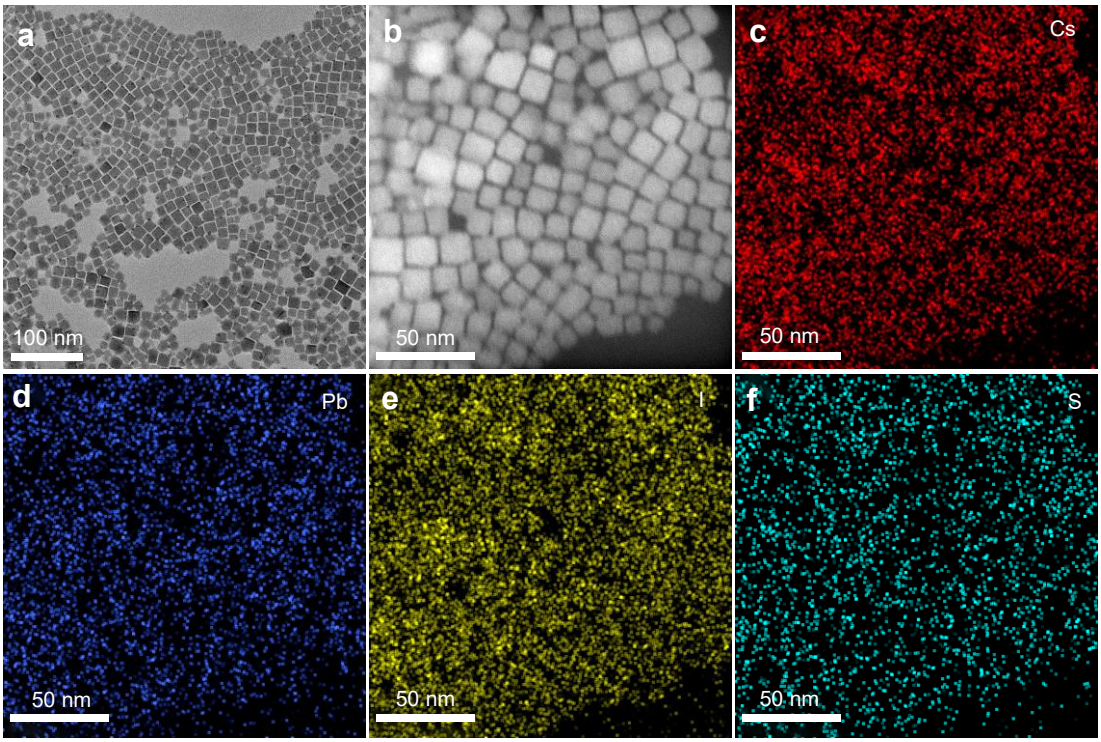

Supplementary Fig. 6 | Morphological characterization of treated $CsPbI_3$ QDs. (**a** and **b**) (a) TEM and (b) HAADF-STEM images of treated QDs. (**c** to **f**) EDS mapping of (c) Cs, (d) Pb, (e) I, and (f) S.

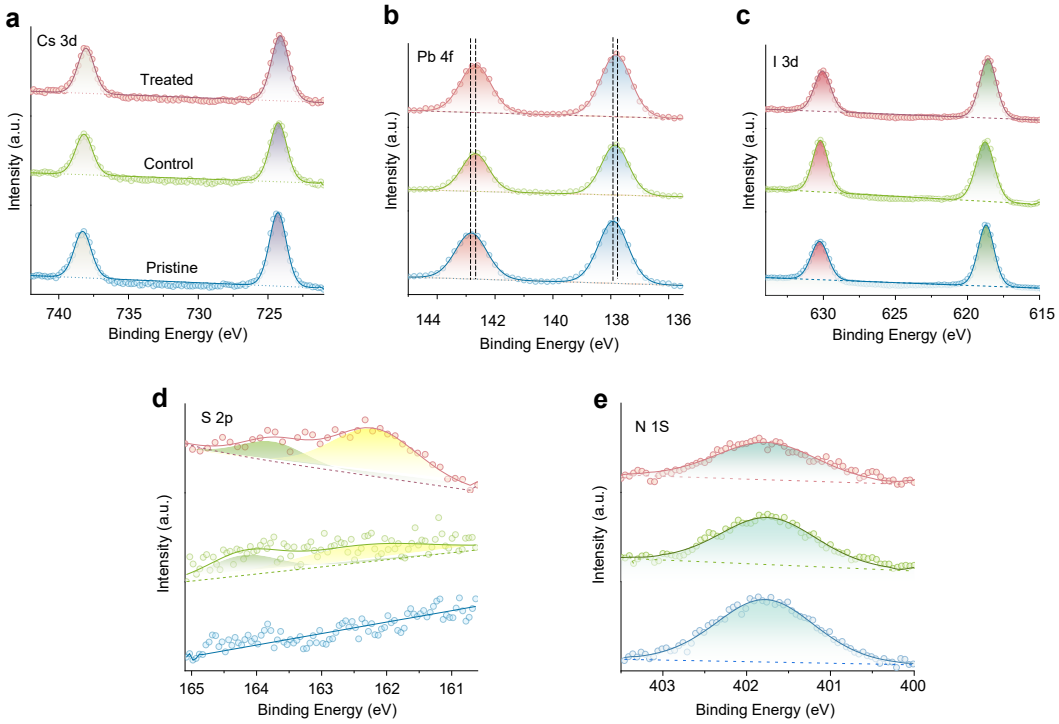

Supplementary Fig. 7 | XPS characterization. XPS spectra of $CsPbI_3$ QDs: (**a**) Cs 3d, (**b**) Pb 4f, (**c**) I 3d, (**d**) S 2p, (**e**) N 1s.

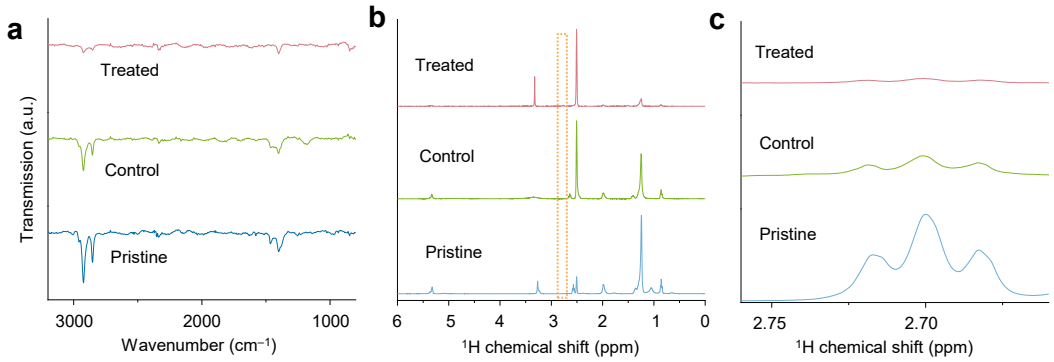

Supplementary Fig. 8 | FTIR and NMR characterization. (**a**) FTIR spectra of $CsPbI_3$ QDs. (**b**) ^1H NMR spectra of $CsPbI_3$ QDs. (**c**) Local magnified ^1H NMR spectra of $CsPbI_3$ QDs.

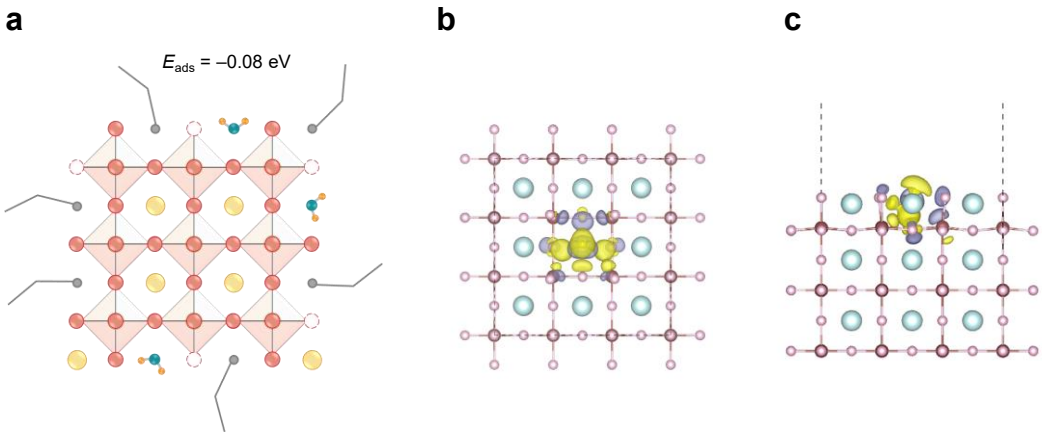

Supplementary Fig. 9 | Theoretical calculations. (**a**) Adsorption energy of H_2S adsorbed on V_{Cs}. (**b** and **c**) Differential charge density of H_2S at V_{Cs}, top view (b), side view (c). These computational results, together with the data shown in Fig. 1e, collectively demonstrate that H_2S adsorption is energetically less favorable at V_{Cs} than at V_I, despite being thermodynamically feasible at both sites.

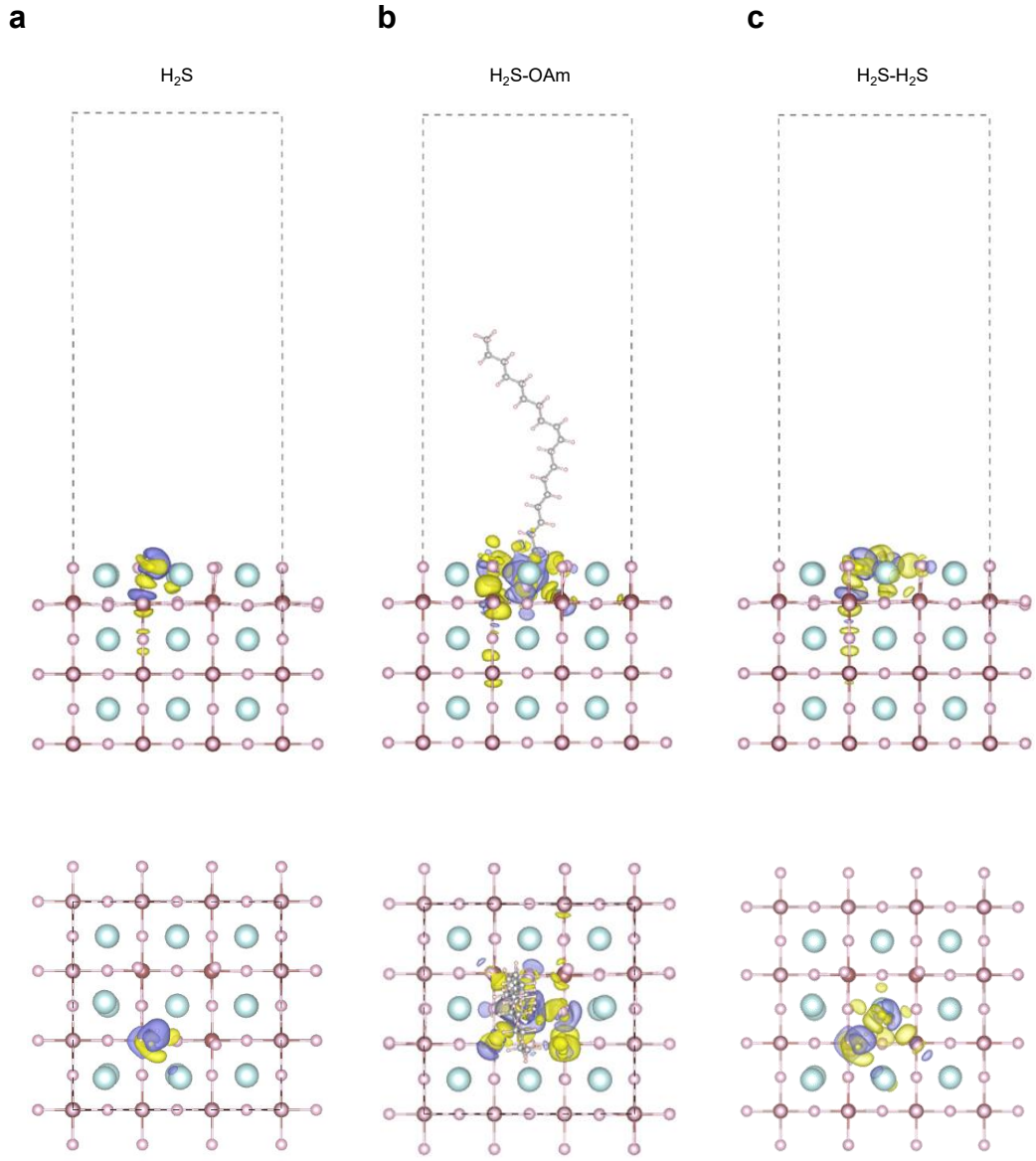

Supplementary Fig. 10 | Differential charge density calculations. (**a**) Differential charge density of H_2S at V_I. (**b**) Differential charge density of H_2S adsorption at V_I and desorption of adjacent OAm. (**c**) Differential charge density of H_2S dimer adsorbed at V_I and V_{Cs}. H_2S adsorption at V_I sites induces Pb–S bond formation and significant local charge redistribution. This rearrangement subsequently weakens the OAm–I binding, thereby facilitating ligand exchange where adjacent OAm is replaced by another H_2S molecule.

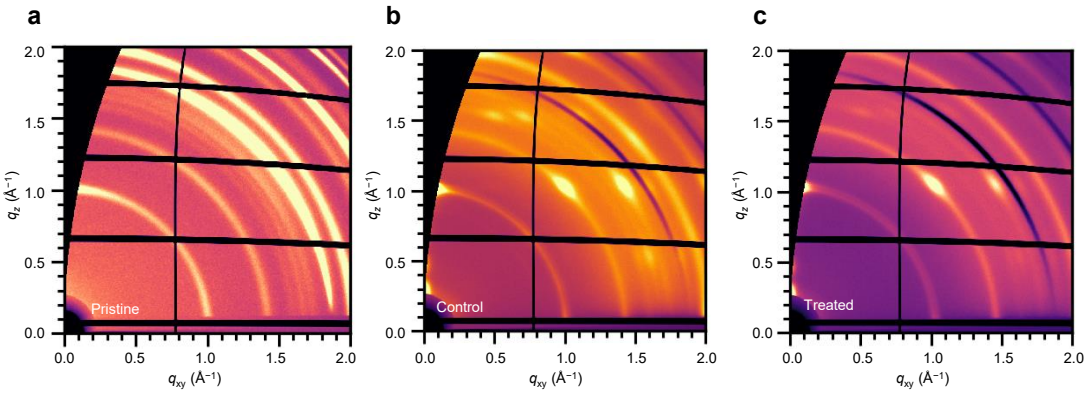

Supplementary Fig. 11 | Spatial homogeneity characterization. (**a** to **c**) Two-dimensional GIWAXS diffraction patterns of (a) pristine, (b) control, and (c) treated QD films at an incident angle of 0.20°. The GIWAXS detection depth is changed by adjusting the X-ray incident angle (0.05° to 0.50°).

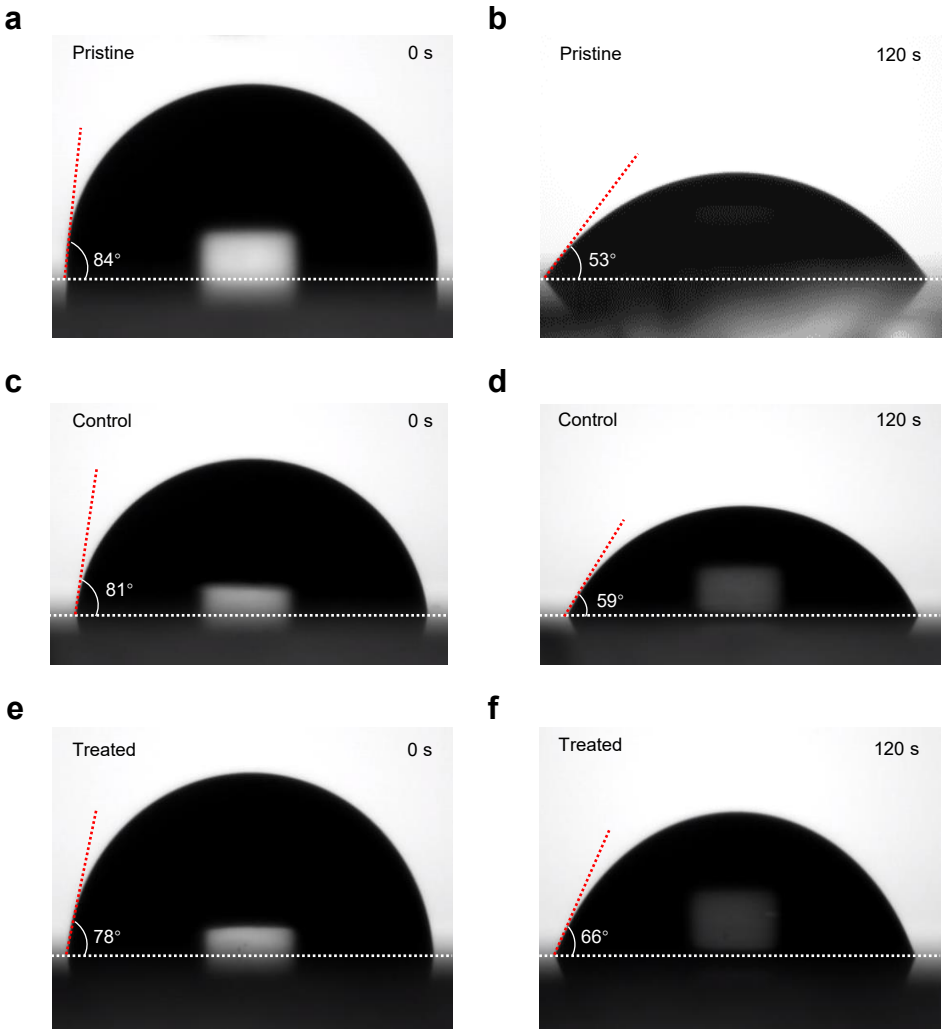

Supplementary Fig. 12 | Environmental Stability of $CsPbI_3$ QD films. (**a** to **f**) Images of water droplets on the surface of (a and b) pristine, (c and d) control, and (e and f) treated QD films at different water-loading times.

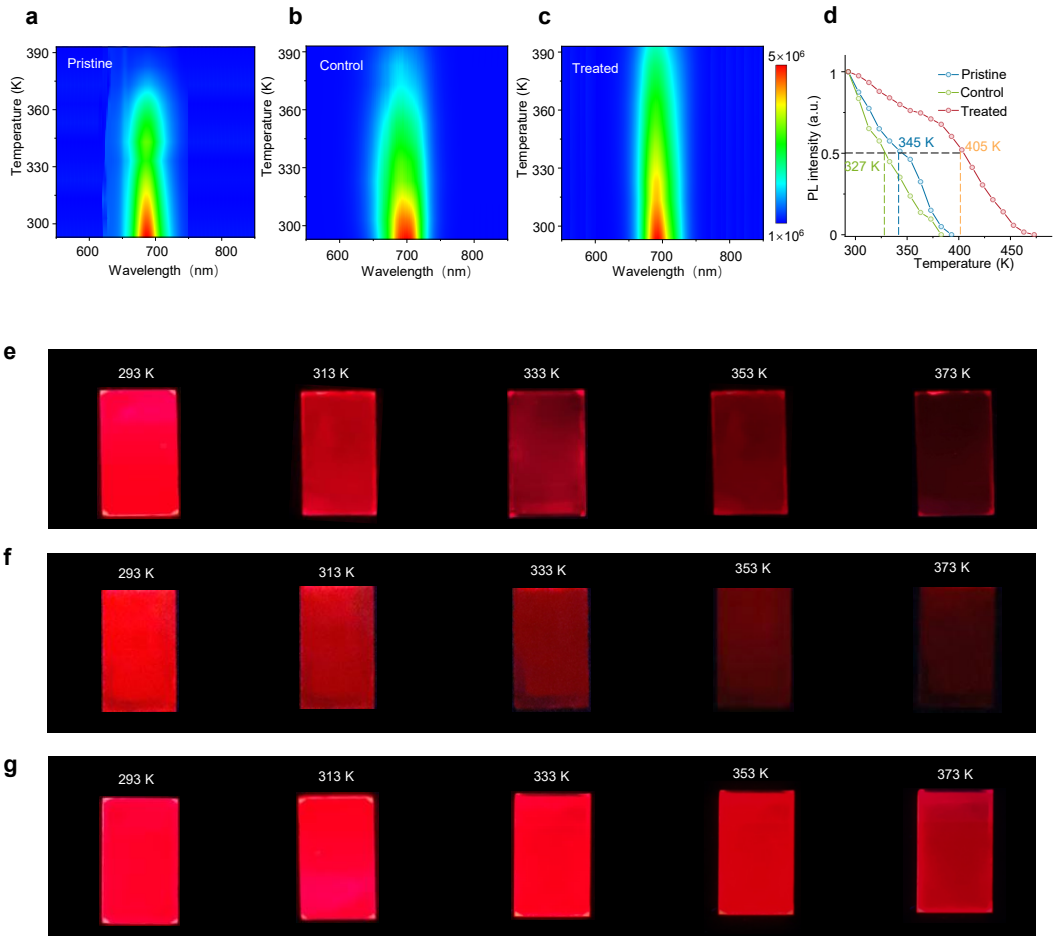

Supplementary Fig. 13 | Thermal stability. (**a** to **c**) Pseudocolor maps illustrating temperature-dependent PL intensities of (a) pristine, (b) control, and (c) treated $CsPbI_3$ QD films. (**d**) PL intensities as a function of temperature. (**e** to **g**) Photographs of (e) pristine, (f) control, and (g) treated films under UV irradiation at different temperatures.

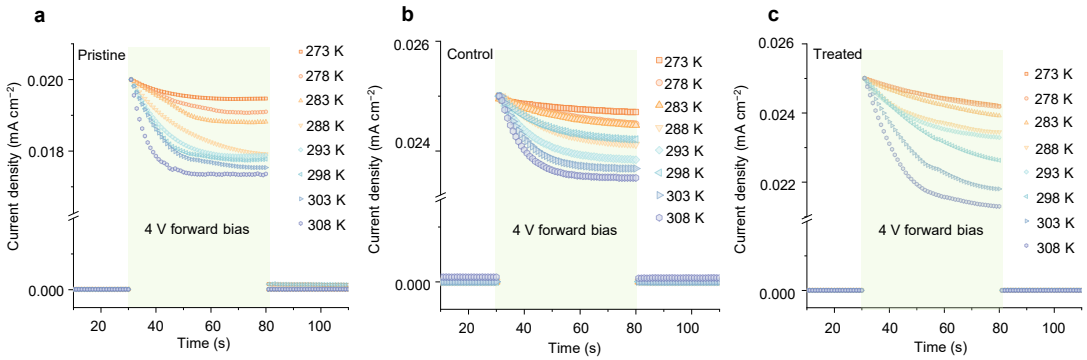

Supplementary Fig. 14 | Ion migration barriers. (**a** to **c**) Arrhenius plots of conductivity for (a) pristine, (b) control, and (c) treated $CsPbI_3$ QD based devices under dark conditions.

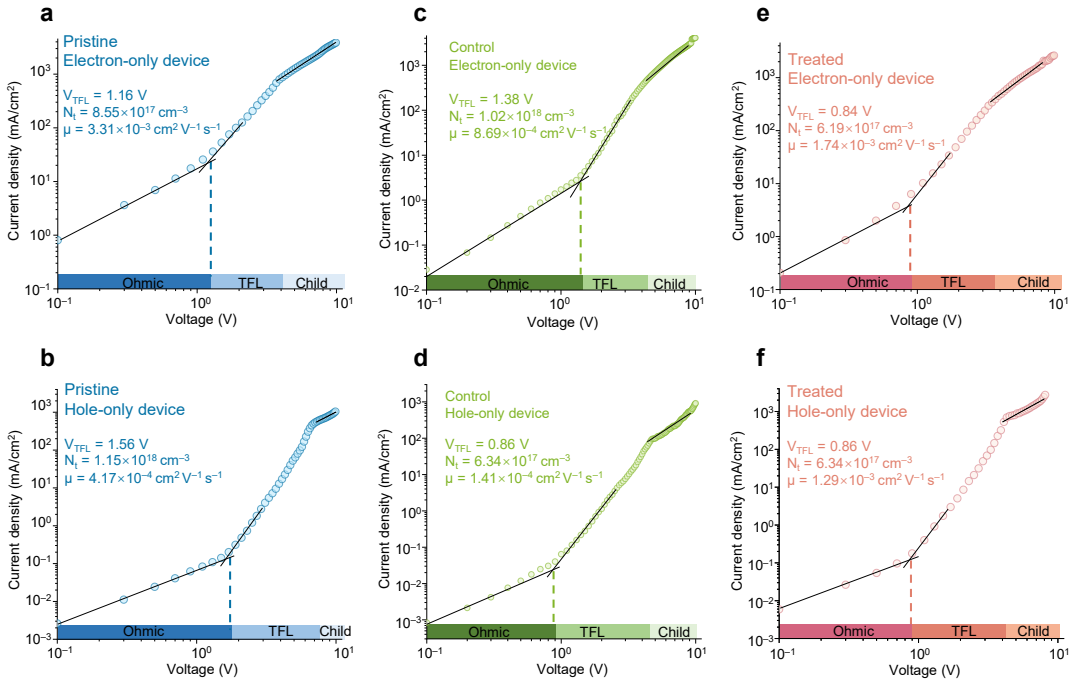

Supplementary Fig. 15 | SCLC characterization. (**a** to **f**) (a, c, e) Electron-only and (b, d, f) hole-only devices based on $CsPbI_3$ QDs with the structures of ITO/QDs/TPBi/LiF/Ag and ITO/PEDOT:PSS/Poly-TPD/QDs/Ag, respectively. The treated devices demonstrate significantly suppressed trap-state density along with balanced electron and hole mobilities.

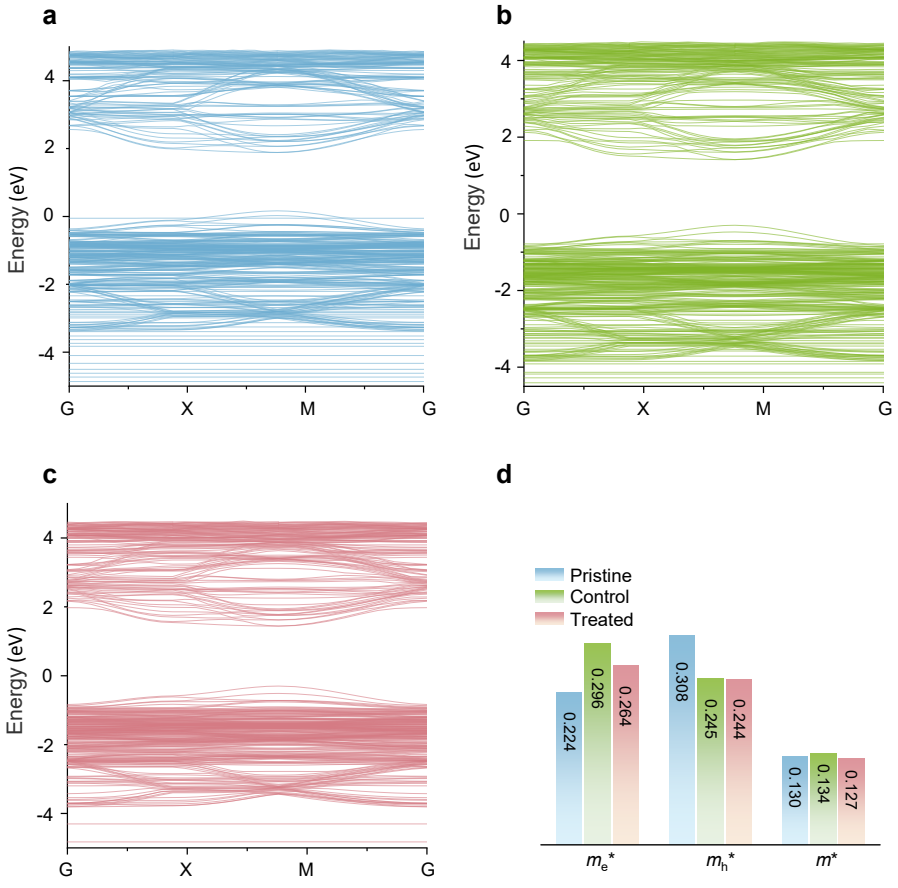

Supplementary Fig. 16 | Band structure calculation. (**a** to **c**) Band structures of (a) pristine, (b) control, and (c) treated $CsPbI_3$ QDs. (**d**) Calculated m_e^*, m_h^*, and m^* of $CsPbI_3$ QDs.

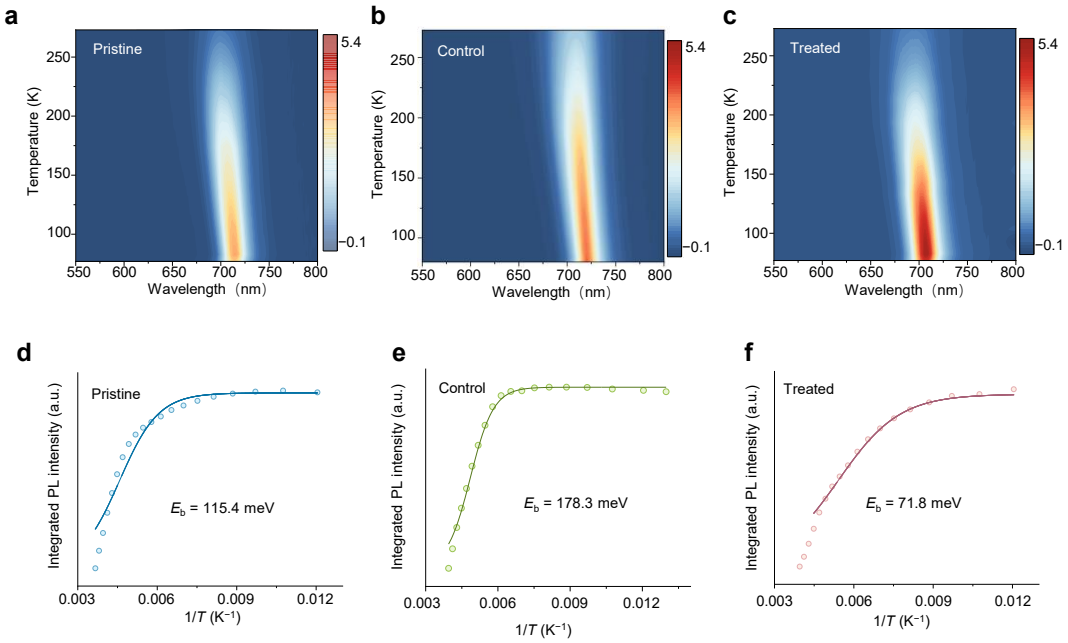

Supplementary Fig. 17 | Exciton binding energy characterization. (**a** to **c**) Pseudocolor maps illustrating temperature-dependent PL intensities of (a) pristine, (b) control, and (c) treated $CsPbI_3$ QD films. (**d** and **f**) Integrated PL intensities as a function of temperature for (d) pristine, (e) control, and (f) treated $CsPbI_3$ QD films.

E_b was extracted by fitting the integrated PL intensity versus reciprocal temperature with an Arrhenius model:

$$I(T) = \frac{I_0}{1 + A \exp\left(-\frac{E_b}{k_B T}\right)}$$

where I_0 is the PL intensity at 0 K, A is a constant, and k_B is the Boltzmann constant. The treated sample shows a reduced E_b of 74.6 meV, revealing weakened Coulombic electron–hole attraction, which can suppress Auger recombination.

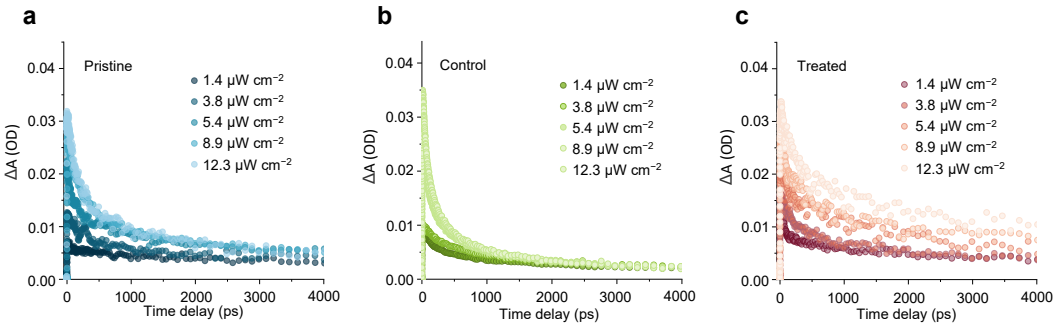

Supplementary Fig. 18 | Carrier dynamics characterization. (**a** to **c**) Transient absorption bleach recovery kinetics of (a) pristine, (b) control, and (c) treated QD films.

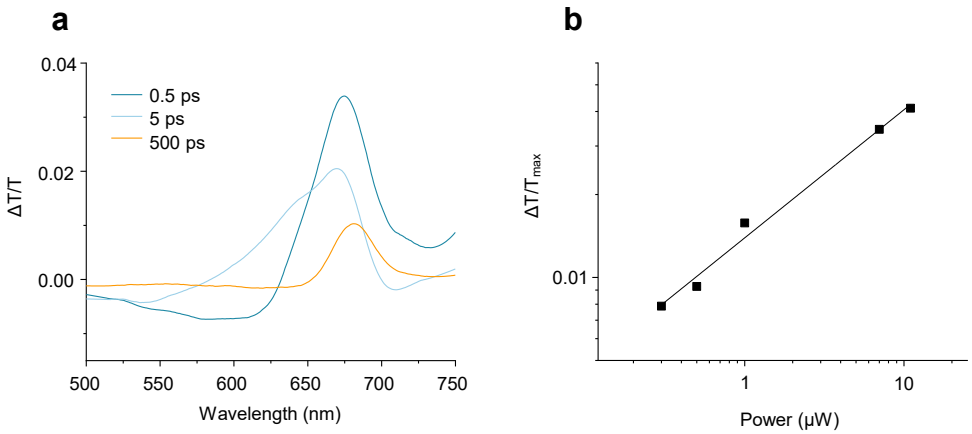

Supplementary Fig. 19 | Transient absorption spectra. (**a**) Typical transient absorption spectra of the treated-QD film at different time delays. The strong positive peak at 680 nm represents ground-state bleaching, used to track carrier density. (**b**) Curves showing the initial transient absorption bleaching signal as a function of pump power.

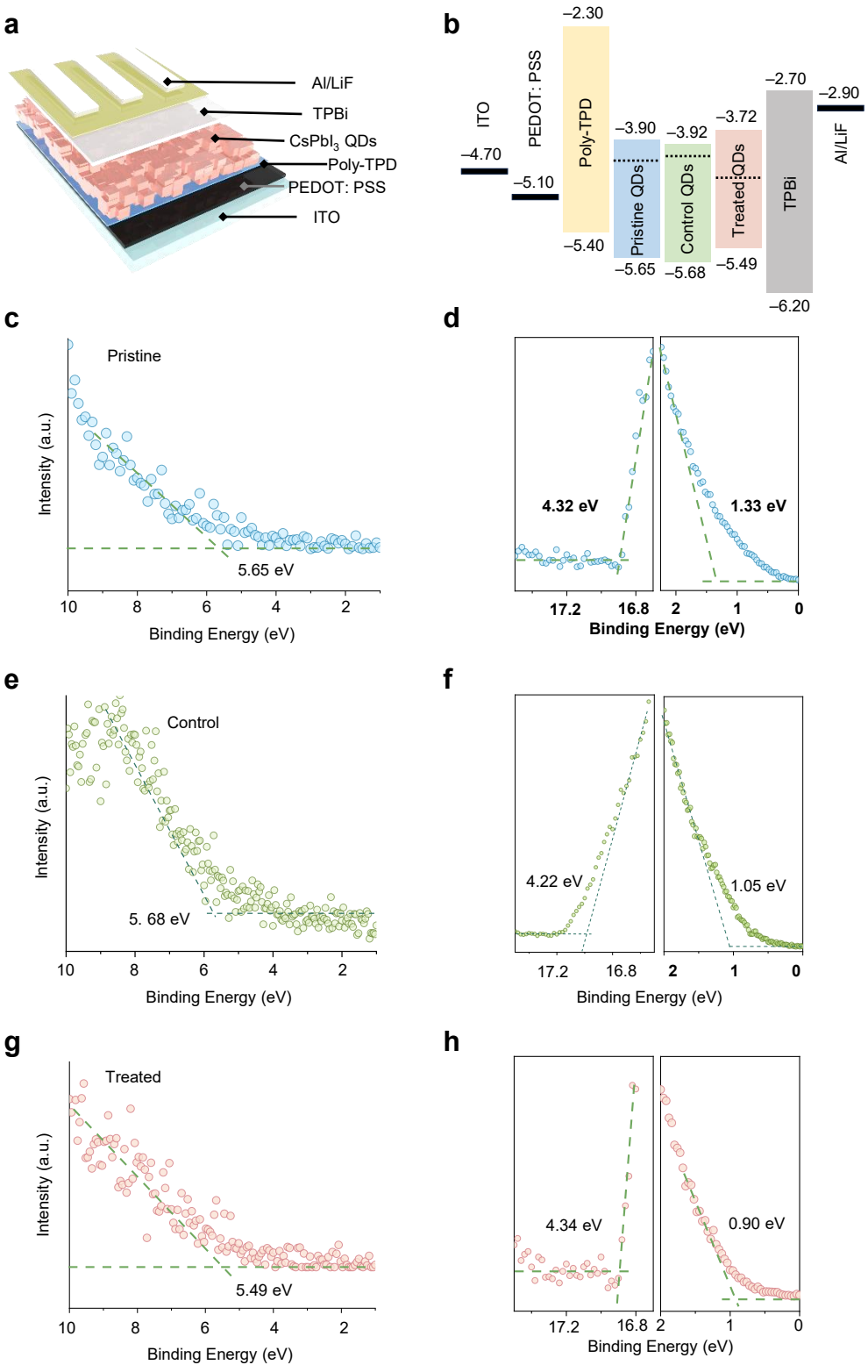

Supplementary Fig. 20 | Energy level structure. (**a**) Device structure of the LEDs. (**b**) Schematic diagram of energy levels. (**c** to **h**) UPS spectra of (c and d) pristine, (e and f) control, and (g and h) treated QD film.

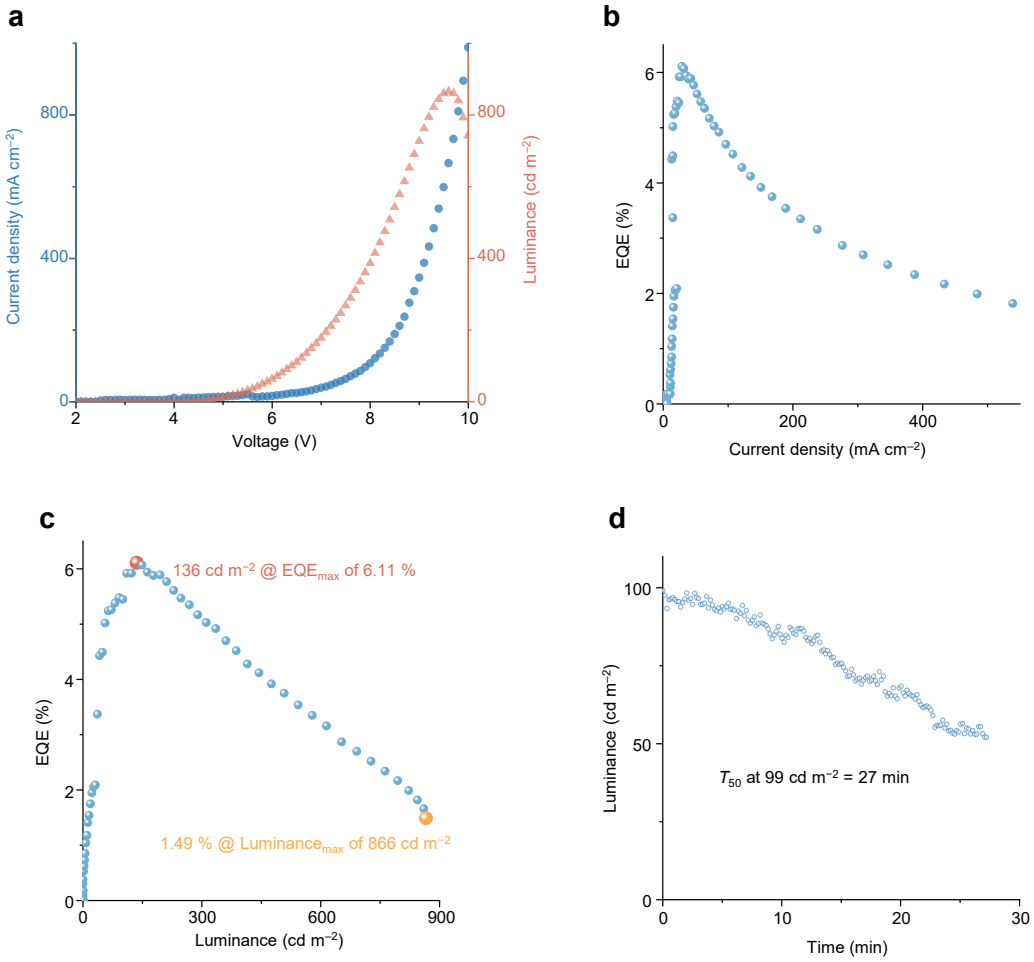

Supplementary Fig. 21 | Performance of pristine device. (**a**) *J*-*V*-*L* curve. (**b**) *J*-EQE curve. (**c**) *L*-EQE curve. (**d**) T_{50} operational lifetime (L_0 = 99 cd m^{-2}).

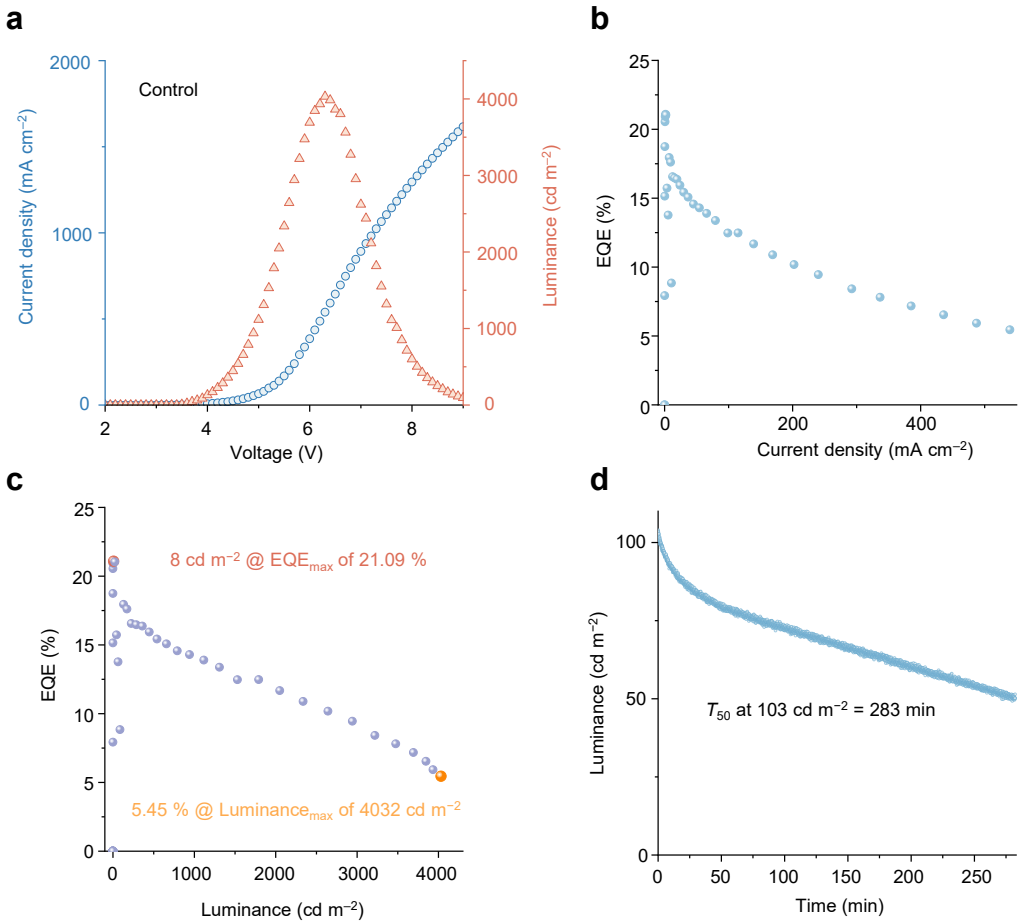

Supplementary Fig. 22 | Performance of control device. (**a**) *J*-*V*-*L* curve. (**b**) *J*-EQE curve. (**c**) *L*-EQE curve. (**d**) T_{50} operational lifetime (L_0 = 103 cd m^{-2}).

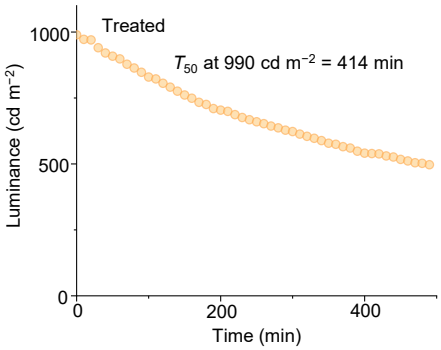

Supplementary Fig. 23 | LED performance. T_{50} operational lifetime of treated LEDs (L_0 = 990 cd m^{-2}).

Supplementary Table 1 | EQE of ten treated devices at various current densities.

LEDs	J (mA cm^{-2})	EQE (%)	J (mA cm^{-2})	EQE (%)	J (mA cm^{-2})	EQE (%)
1	102.49	21.60	298.92	24.75	501.75	18.31
2	96.42	27.92	301.64	26.36	523.18	19.90
3	102.76	27.58	293.60	26.08	516.67	19.63
4	103.39	26.76	304.18	27.93	501.88	21.34
5	104.39	27.60	299.47	26.17	506.94	19.16
6	105.88	26.91	309.20	21.93	511.85	16.01
7	106.14	27.51	299.71	24.41	484.06	18.87
8	104.27	24.49	305.62	25.10	491.10	22.61
9	110.68	22.33	299.24	29.14	497.10	22.61
10	103.83	29.14	295.23	24.04	501.49	18.60

Supplementary Table 2 | L @ EQE_{max} and EQE @ L_{max} of ten treated devices.

LEDs	L @ EQE_{max} (cd m^{-2})	EQE_{max} (%)	EQE @ L_{max} (%)	L_{max} (cd m^{-2})
1	2401.46	28.20	14.82	10102.2
2	1995.96	27.72	14.65	8591.38
3	4182.72	26.32	15.76	8181.35
4	3147.47	26.99	15.08	11194.14
5	2860.94	28.60	15.62	8845.62
6	5891.85	29.16	15.4	10423.52
7	3209.13	28.05	17.05	9145.00
8	4119.78	25.89	18.31	8027.68
9	6374.30	29.47	19.43	9784.87
10	1089.14	30.71	16.36	7779.40

Table S3. *L* at EQE_{max} of Ref. 1-8.

Perovskite	EQE_{max} (%)	*L* @ EQE_{max} (cd m^{-2})	Ref.
$CsPbI_{3-x}Br_x$	21.83	40.91	1
$CsPbI_3$	25.01	96.93	2
$CsPbI_3$	28.44	2.40	3
$CsPb(Br/I)_3$	24.72	36.26	4
$CsPbI_3$	20.79	1.47	5
$CsPbI_3$	25.36	87.33	6
$CsPbI_3$	26.05	1.47	7
$CsPbI_3$	28.75	57.84	8
$CsPb(Br/I)_3$	28.86	6.59	9
$CsPbI_3$	30.75	8.75	10
$CsPbI_3$	31.48	2.70	11
$CsPbI_3$	30.71	1089.14	This work

Table S4. EQE at various *L* of Ref. 1-8.

Perovskite	EQE @ ~1000 cd m^{-2}		EQE @~3000 cd m^{-2}		EQE @ ~5000 cd m^{-2}		Ref.
	EQE (%)	*L* (cd cm^{-2})	EQE (%)	*L* (cd cm^{-2})	EQE (%)	*L* (cd cm^{-2})	
$CsPbI_{3-x}Br_x$	10.36	935	/	/	/	/	1
$CsPbI_3$	17.95	1017	10.15	3016	6.90	4894	2
$CsPbI_3$	15.75	959	5.45	2992	/	/	3
$CsPb(Br/I)_3$	22.30	921	19.28	2822	17.50	5185	4
$CsPbI_3$	4.28	1380	/	/	/	/	5
$CsPbI_3$	17.08	1001	10.51	2928	/	/	6
$CsPbI_3$	16.19	1107	10.01	2971	/	/	7
$CsPbI_3$	21.03	1312	11.80	3050	/	/	8
$CsPb(Br/I)_3$	24.83	1333	22.83	2720	19.20	5396	9
$CsPbI_3$	17.98	1011	/	/	/	/	10
$CsPbI_3$	16.2	926	/	/	/	/	11
$CsPbI_3$	30.65	958	27.94	3070	25.01	5171	This work

Table S5. EQE at various *J* of Ref. 1-8.

Perovskite	EQE @~10 mA cm^{-2}		EQE @~100 mA cm^{-2}		EQE @~300 mA cm^{-2}		EQE @~500 mA cm^{-2}		Ref.
	EQE (%)	J (mA cm^{-2})	EQE (%)	J (mA cm^{-2})	EQE (%)	J (mA cm^{-2})	EQE (%)	J (mA cm^{-2})	
$CsPbI_{3-x}Br_x$	10.36	8.45	/	/	/	/	/	/	1
$CsPbI_3$	17.11	9.98	6.90	98.20	/	/	/	/	2
$CsPbI_3$	17.87	10.51	5.45	100.95	2.02	306.41	1.05	493.31	3
$CsPb(Br/I)_3$	21.41	10.74	14.18	93.66	8.22	296.58	5.32	509.45	4
$CsPbI_3$	8.35	8.27	3.39	101.06	/	/	/	/	5
$CsPbI_3$	16.72	9.75	6.22	96.04	/	/	/	/	6
$CsPbI_3$	14.97	9.81	5.86	70.67	/	/	/	/	7
$CsPbI_3$	21.03	7.13	2.97	75.76	/	/	/	/	8
$CsPb(Br/I)_3$	21.82	11.56	9.17	98.44	2.08	311.55	/	/	9
$CsPbI_3$	20.07	9.38	9.83	98.06	0.51	291.62	0.10	508.35	10
$CsPbI_3$	13.15	9.83	2.22	110.39	0.00	309.08	/	/	11
$CsPbI_3$	30.37	9.52	29.14	103.83	24.04	295.23	18.59	501.49	This work

References

1 Xie, M. *et al.* Suppressing ion migration of mixed-halide perovskite quantum dots for high efficiency pure-red light-emitting diodes. *Adv. Funct. Mater.* **33**, 2300116 (2023).

2 Guo, J. *et al.* High efficiency and low roll-off pure-red perovskite LED enabled by simultaneously inhibiting auger and trap recombination of quantum dots. *Nano Lett.* **24**, 6410-6416 (2024).

3 Li, H. *et al.* Nanosurface-reconstructed perovskite for highly efficient and stable active-matrix light-emitting diode display. *Nat. Nanotechnol.* **19**, 638-645 (2024).

4 Li, H. *et al.* Thermal management towards ultra-bright and stable perovskite nanocrystal-based pure red light-emitting diodes. *Nat. Commun.* **15**, 6561 (2024).

5 Xie, M. *et al.* High-efficiency pure-red perovskite quantum-dot light-emitting diodes. *Nano Lett.* **22**, 8266–8273 (2022).

6 Xie, M. *et al.* Efficient and stable pure-red perovskite LED based on uniform arrangement strongly confined quantum-dot film. *ACS Energy Lett.* **9**, 4003-4008 (2024).

7 Li, Y. *et al.* Stable and efficient $CsPbI_3$ quantum-dot light-emitting diodes with strong quantum confinement. *Nat. Commun.* **15**, 5696 (2024).

8 Kong, L. *et al.* Fabrication of red-emitting perovskite LEDs by stabilizing their octahedral structure. *Nature* **631**, 73-79 (2024).

9 Feng, Y. *et al.* Surface Compensation Principles of Soft-Lattice Nanocrystals toward High-Performance Electroluminescence. *Adv. Mater.* **37**, e10886 (2025).

10 Wang, J. *et al.* Extending the temperature and time operating windows of $CsPbI_3$ quantum dots for scalable synthesis for LEDs. *Angew. Chem. Int. Ed.* **65**, e3302558 (2026).

11 Yao, J., Xu, Y., Guo, W., Yao, S. & Song, J. Recoverable defect suppression in

$CsPbI_3$ quantum dots for efficient and stable pure-red light-emitting diodes. *ACS Nano* **20**, 4979–4988 (2026).